Digital elevation model construction from structured topographic data: The DEST algorithm

Massimiliano Favalli and M. Teresa Pareschi
Istituto Nazionale di Geofisica e Vulcanologia, Pisa, Italy

Received 12 March 2004; revised 26 June 2004; accepted 17 August 2004; published 9 November 2004.

[1] An algorithm, Determination of Earth Surface Structures (DEST), is presented to reconstruct digital terrain models of complex landforms from topographic data, such as contour lines and spot heights. The algorithm provides a triangular irregular network (TIN) of the source data, based on a modified Delaunay approach. Delaunay triangulation can introduce artificial terraces from a nonrandom distribution of input points such as a sampled contour line. The algorithm proposed here constructs the three-dimensional principal skeletons of these artificial flat areas, eliminating the unwanted effects of contour lines. The algorithm can also be applied to topographic data from a variety of mixed sources such as photogrammetric information, radar altimetry measurements, and traditional contour lines. The sparse fine-surface structures present in the source data are preserved, allowing accurate morphological evaluations, tectonic lineament extraction, and volume estimation. A methodology (D-DEST) to easily derive, from a TIN computed by DEST, the drainage path and the catchment areas is also presented. A comparison of DEST with other methodologies is performed. It results that our approach does not introduce sensible biased effects in slopes, aspects, drainage network, and catchment areas. The evolution of the upper cone of Vesuvius volcano (Italy) during the last century, as derived from historical cartography, is presented as an application of DEST. The algorithm implemented in C can be requested at DEST_pareschi@pi.ingv.it. *INDEX TERMS:* 1824 Hydrology: Geomorphology (1625); 1625 Global Change: Geomorphology and weathering (1824, 1886); 3299 Mathematical Geophysics: General or miscellaneous; 8494 Volcanology: Instruments and techniques; *KEYWORDS:* digital elevation model, morphology, Vesuvius, drainage network, watershed

Citation: Favalli, M., and M. T. Pareschi (2004), Digital elevation model construction from structured topographic data: The DEST algorithm, *J. Geophys. Res.*, *109*, F04004, doi:10.1029/2004JF000150.

1. Introduction

[2] A model of the height of a portion Earth's surface can be of fundamental importance in many geophysical, geological, and geographical studies, such as morphological analyses, the assessment of hazard and risk for terrain-controlled phenomena, the study of lineaments and faults, and volume estimations [*Zhang and Montgomery*, 1994; *Guzzetti and Reichenbach*, 1994; *Martz and Garbrecht*, 1995; *Stevens et al.*, 1999; *Favalli et al.*, 1999; *Kuhni and Pfiffner*, 2001; *Pareschi et al.*, 2000a, 2002; *Stevens et al.*, 2003; *Kirby et al.*, 2003]. Different techniques can be used to produce a digital terrain model (DTM), including topographic measurements on the ground, digital aerophotogrammetry, laser scanners and radar, and interpolation from existing maps (e.g., spot heights and contour lines) [*Shearer*, 1990; *Liu et al.*, 1999; *Meyer*, 2000; *Bamber et al.*, 2001; *Davis et al.*, 2001].

[3] Interpolation from point values sampled along contour lines to give the final DTM structure is doubtless the cheapest and/or the only feasible approach in historical cartography or topographic mapping where information on elevation is already available. It is currently one of the most popular techniques used to obtain DTMs for large regions. It is crucial in the generation of a DTM to avoid bias and the introduction of artificial features when the input points exhibit a structured pattern [*Lee*, 1991; *Wood and Fisher*, 1993; *Carrara et al.*, 1997; *Liu and Jezek*, 1999; *Almansa et al.*, 2002] since the reliability of the application depends on the accuracy of the DTM [*Zhang and Montgomery*, 1994; *Wolock and Price*, 1994; *Florinsky*, 1998; *Pareschi et al.*, 2000a; *Stevens et al.*, 1999, 2003].

[4] This paper proposes a technique to reconstruct a DTM based on a triangular irregular network (TIN) structure. The most widely technique used to built a TIN from a set of sparse points is the Delaunay algorithm [*Macedonio and Pareschi*, 1991], identifying, among all the possible triangulations, that one where, in every triangle, the minimum angle is the maximum possible one. In the constrained Delaunay approach, commonly adopted when the input points are along sampled contour lines, no triangulation can occur across a contour line. In both cases, artificial flat areas are introduced where contour lines present an high

0148-0227/04/2004JF000150$09.00

curvature radius. Our algorithm identifies these artificially flat areas introduced in the DTM, builds a skeleton for them, interopolates z values along the skeleton, and retriangularizes the structure based on the previous input information and on the new breaklines and elevations. Our algorithm, named Determination of Earth Surface Structures (DEST), provides, in general, terrain reconstruction from sparse points, but it becomes a powerful tool when the source points are digital values along contour lines so that their distribution in the plane is not random. The efficacy of DEST is discussed by comparison with other interpolation techniques. In a specific paragraph the potentiality of DEST to compute morphological features, in particular, ridges and gullies, drainage network, channel slopes, and upstream contributing areas, is discussed. In section 7 an application of DEST is presented to reconstruct the upper cone of the Vesuvius volcano (southern Italy) during the last century, when only historical maps and contour lines are available to support quantitatively the morphological evolution and volume changes of that volcano.

2. Delaunay and the Constrained Delaunay Triangulation

[5] A number of different data structures have been used to store and display topographic structures, but the most commonly used is the elevation matrix structure based on a square grid (digital elevation model (DEM)) and the triangular irregular network (TIN) structure.

[6] In a TIN structure, input planar points (each one characterized by two planar coordinates x_p, y_p) are connected in a network of triangles. In space the terrain surface is approximated by a set of triangular facets where the altimetry information (z_p value) of each node (x_p, y_p) is used to determine the local triangular facet orientation. Compared with a grid structure, the advantages of a TIN structure are as follows [*Wood and Fisher*, 1993; *Mitasova et al.*, 1996; *Carrara et al.*, 1997; *Meyer*, 2000]: (1) the reduction of redundant data in areas with uniform relief or, vice versa, the maintenance of high detail where dictated by relief and gradient; (2) a simple derivation of morphological parameters such as slope angle and maximum gradient; (3) no anisotropies associated, as in the case of a DEM, with the vertical, horizontal, and diagonal directions of the mesh; (4) in the altimetric model, incorporation of auxiliary information such as gullies, ridges and faults.

[7] The best known and most widely used triangulation technique is that based on the Delaunay algorithm [*Watson*, 1981; *Preparata and Shamos*, 1985; *McCullagh*, 1988; *Macedonio and Pareschi*, 1991; *Rebay*, 1993; *Mavriplis*, 1995; *Stevens et al.*, 1999], where the input points are connected to form a set of triangles, the minimum angle of which is the maximum one in all the triangulations. This algorithm, which can be extended to 3 (or n) dimensions using tetrahedral meshes to deal with three-dimensional (3-D) geographical object reconstruction such as underground profiles and aquifers [*Golias and Dutton*, 1997; *Li*, 2003], does, however, introduce bias effects if the input points are not randomly distributed.

[8] As indicated by the great number of interpolation techniques available in the literature to produce TINs or DEMs, the interpolation of sparse nonrandom elevation points (i.e., elevation points from digitized map contours) to coherent and structurally significant morphological terrain models remains a central problem. It is often solved roughly or heuristically [*Watson*, 1992; *Li*, 1994; *Mitas and Mitasova*, 1999; *Albani and Klinkenberg*, 2003].

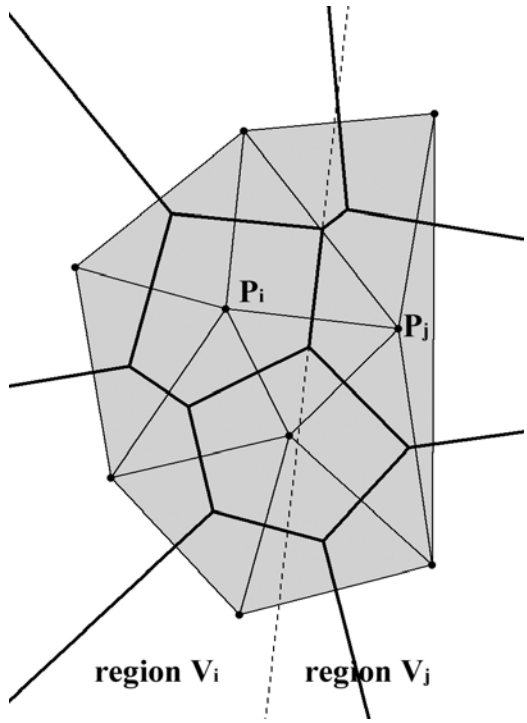

Figure 1. Voronoi regions (thick lines) and associated Delaunay triangulation for nine generating points. Tile edges (bold) lie on the axes of the sides of the Delaunay triangles. Points within a tile are closer to the tile's generating point than to any other generating point. The dotted line is the axis of segment P_iP_j and divides the plane into two region V_i and V_j.

[9] The first systematic approach to the problem of connecting a set of points to reconstruct 2-D and 3-D meshes was that of Dirichlet and dates back to 1850. He proposed subdividing a given domain into a set of convex polygons [*Preparata and Shamos*, 1985]. According to Figure 1, given two points P_i and P_j in a plane, the axis of the segment P_iP_j divides the plane into two regions, V_i and V_j. Region V_i contains all, and only, the points closer to P_i than to P_j. If we have more points, we can easily extend this concept by saying that V_i is the region assigned to P_i so that each point belonging to V_i is closer to P_i than to any other point. The subdivision of a space into regions defined as the nearest neighborhoods to a set of distinct points is called Dirichlet tessellation.

[10] In the plane, this process applied to a closed domain generates a set of distinct convex polygons called a Voronoi diagram (Figure 1). If all the pairs of points (P_i, P_j), sharing a side of a Voronoi polygon are connected, we obtain a triangulation of the convex region containing these points, known as the Delaunay triangulation (DT).

[11] The Delaunay triangulation shows some interesting features [*Watson*, 1981; *Preparata and Shamos*, 1985]: (1) given a triangle (P_i, P_j, P_k) belonging to a Delaunay

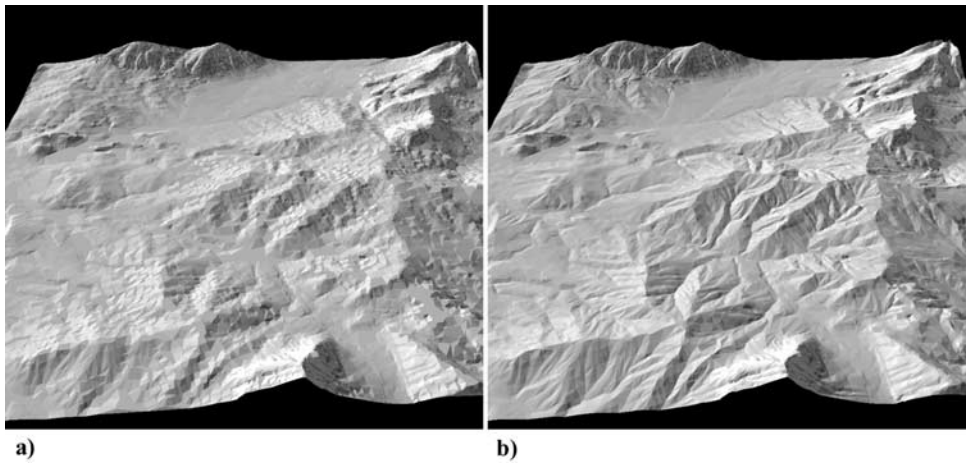

Figure 2. Three-dimensional (3-D) perspective views of a mountain region, reconstructed by (a) a CDT and by (b) the DEST algorithm. In areas subtended by contour lines with an high curvature a DT or a CDT can introduce false morphologies (flat terraces, Figure 2a). The DEST algorithm eliminates the flat triangles (Figure 2b) by the computation of ridges and gullies.

triangulation of a set of generating input points, no other point of the generating set is internal to the circle defined by P_i, P_j, P_k; (2) in the Delaunay triangulation the minimum angle of all the triangles is the maximum outside of all the triangulations. Feature 1 guarantees that the ''nearest'' points are joined together, while feature 2 means that the triangles are as ''equilateral'' as possible so that ''distal'' information is not linked together.

[12] The Delaunay triangulation can be applied to construct a TIN from a set of points coming from the vectorization of contour lines and isolated points of a topographic map. In space the triangles are those defined by their three points (z values from spot heights and contour lines); their projection onto the horizontal plane x-y is the Delaunay set. It is always possible to deduce a DEM from a TIN. At the generic grid node P of planar coordinates (x_p, y_p) the corresponding z_p value can be deduced from the plane defined by the three vertices of the triangle enclosing P.

[13] When a TIN is generated by a DT of the digitized points from topographic contour lines to represent the surface of the landscape, in some cases, artifacts may appear: (1) a number of flat triangles could be generated where nodes of equal height (belonging to the same contour line) are joined, forming horizontal artificial terraces along the contour [*Stevens et al.*, 1999, 2003]. The flat regions are particularly liable to occur where the curvature of the contour lines is high (Figures 2a and 3b); (2) the Delaunay approach can join points belonging to different noncontiguous contour lines, crossing the intermediate contour line; (3) a DT does not force given segments (faults or other morphological features, e.g., ridges) to become edges of triangles (breaklines).

[14] The concept of constrained Delaunay triangulation (CDT) is introduced in order to prevent some false features from appearing (the last two requirements just listed above). A CDT of a set of points and segments is similar in all respects to a Delaunay triangulation, except that the input segments are forced to be triangle edges. Obviously, a CDT may not always satisfy the criteria for a Delaunay triangulation.

3. Removal of False Flat Patches in the Constrained Delaunay Triangulation (CDT) Using DEST

[15] As already mentioned, a DT or a CDT can introduce local, false flat morphological features related to triangles,

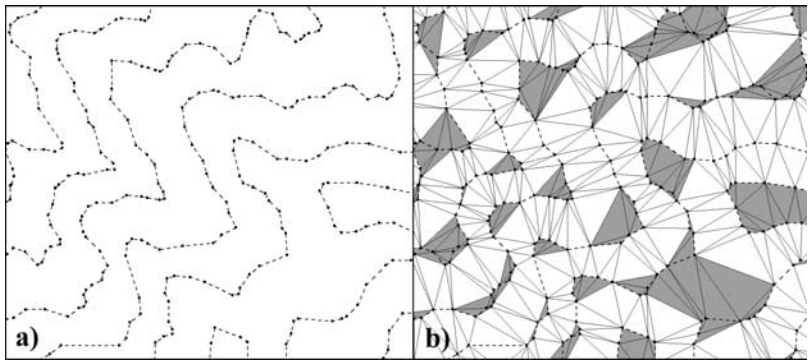

Figure 3. (a) Dots represent the digitalized points in the x,y plane along sampled contour lines (dashed). (b) Flat areas reconstructed by a DT or a CDT outlined as gray triangles. All these triangles have vertices with the same z value since belonging to the same contour line.

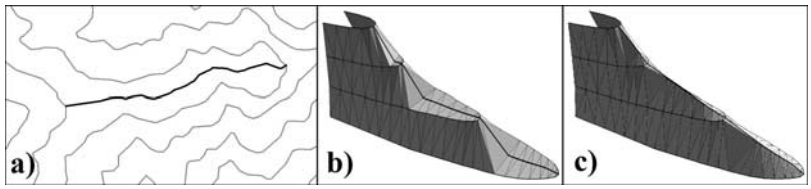

Figure 4. (a) Inferred breakline (bold) reconstructed as the medial axis of a contour line (thinner gray line). (b) A CDT or a DT introduces flat artificial terraces in areas subtended by contour lines with a high curvature. Triangle sides are shown as thin lines. The bold central line is the reconstructed skeleton draped on the morphology. (c) If the height of the skeletal points is interpolated between adjacent contour lines, a 3-D reconstruction is provided.

whose vertices are on the same contour line, occurring, in particular, in areas subtended by contour lines with a high curvature (Figures 3b and 4b). These false horizontal terraces alter all the local morphological features: height, slopes, drainage network, volumes, and maximum slope paths.

[16] In order to avoid the problem, we propose an algorithm, DEST. In the originally flat regions, DEST computes inferred breaklines (IB) and uses them to reconstruct a new local triangulation. These new lines, with heights interpolated between adjacent contour lines, help in the local reconstruction of the ''true'' morphology. Inferred breaklines are assumed locally to be a gully or a ridge (Figures 4a and 4c).

[17] From a geometrical point of view the IBs are computed as the medial line (skeleton), equidistant from the boundary of the region constituted by the local network of flat triangles (Figures 4a–4c). The medial axis of a simple plane polygon has various names, including symmetric axis or skeleton (Sk). The term ''skeleton'' is preferred to indicate the medial axis of a convex region. One of the most picturesque ways of identifying the medial axis is the grassfire transform: imagine igniting all the boundary points of the polygon. If the flame burns inward at a uniform rate, then the quench points where the flame meets and extinguishes itself define the medial axis [*Blum*, 1967]. A mathematically rigorous definition of the skeleton of a plane figure is the following: let R be a plane figure, B its boundary, and P a point in R. The nearest neighbor of P on B is a point M such that there is no other point in B whose distance from P is less than the distance PM. If P has more than one nearest neighbor on B, then P is said to be a skeletal point of R. The union of all skeletal points is called the skeleton or medial axis of R [*Pavlidis*, 1982].

[18] It can be demonstrated that the skeleton of a convex region (in our case the flat areas), whose boundary is constituted by straight segments (the corresponding sampled contour line), is a succession of straight segments and arc of parabolas (see Appendix A). Further, when a sampled contour line is considered, it is necessary to distinguish between the skeleton and the principal skeleton (PS), where artificial noise related to contour line sampling is avoided. Appendix A reports some interesting properties of the medial axes and some further details about the methodology adopted by DEST to determine the skeleton in the special case of sampled contour lines.

[19] About PS, in our case, there is a simple, rapid method for identifying it (see Figure 5). In the flat region created by a DT, even in the most complex cases, only three kinds of triangles can occur, according to the number of sides belonging to the contour line: (1) triangles (dark gray in Figure 5) whose vertices are all consecutive on the same contour line (two sides of the triangle are also two segments of the contour line); (2) triangles (white in Figure 5) that have only two vertices consecutive on the same contour line (one side of the triangle is also a segment of the contour line); and (3) triangles having no side on the contour line (light gray triangles in Figure 5). It is evident from Figure 5 that (1) in a ''light gray'' triangle (LGT) an intersection of three branches of the PS occurs; it is also evident that (2) ''white'' triangles (WHT) are simply crossed by the IB; (3) the common vertex Q_a of two sides (contiguous along the contour line) of a ''dark gray'' triangle (DGT) is a departure-arrival point (DAP). A DAP (of the IB) is a point of local maximum curvature of the contour line, where a branch of the PS departs. The computation of the principal skeleton starts from the DAP of the DGTs; the intersections of the medial axes with the internal sides of triangles are evaluated (i.e., point like Sk_{AB} of Figure 5) until (1) a LGT is encountered where the local branch of the PS connects with other branches of the PS (Figure 5) or (2) a not horizontal triangle is encountered (i.e., the green triangle FEQ_3 of Figure 6, where points E and F belong to a contour line, while point Q_3 belongs to another one). The numerical approximation of the PS is reconstructed by connecting with straight segments all these intersections. In Appendix B a fast method to reduce computational time for PS reconstruction is described in detail.

[20] Points Sk_k of the skeleton are heighted using the values of the two contour lines bounding the flat region. As

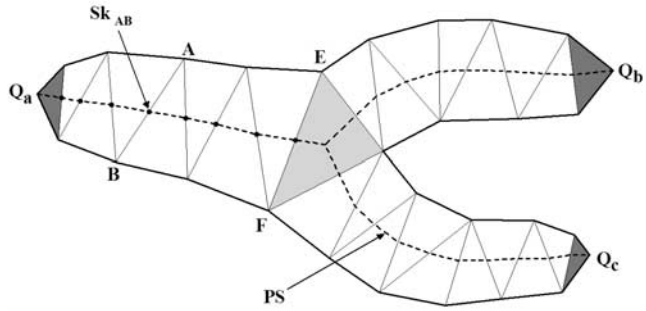

Figure 5. The end points (Q_a, Q_b, Q_c) of the principal skeleton (dashed line) are the vertices of triangles (DGT) with two sides on the contour line. Branching points of the skeleton occur in triangles (LGT) with no side on the contour line.

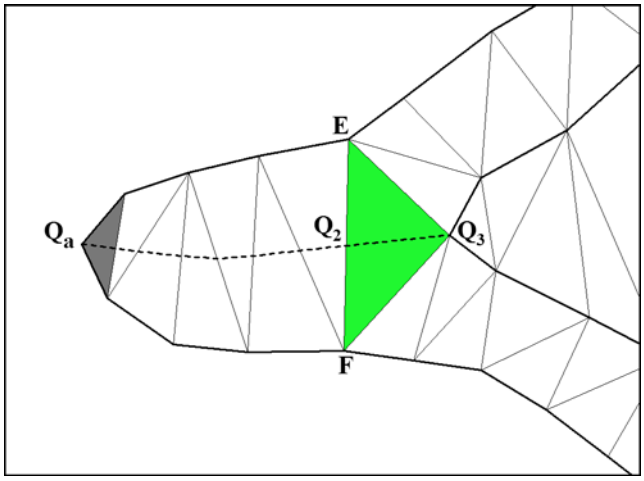

Figure 6. The flat region EQ_aF, built up by triangles with vertices at the same quote, is closed by the (green) triangle FEQ_3, having two vertices at the same height (that of the contour line EQ_aF) and the third vertex Q_3 at the height of the contiguous contour line. The skeleton of the region EQ_aF is the polyline Q_aQ_2, Q_a being a DAP. The skeletal points Sk are assigned height linearly along the skeleton using the values of the two contour lines bounding the flat region (the height of the points Q_a and Q_3).

shown in Figure 6, the flat region EQ_aF, built by some triangles with vertices at the same height, is bordered by a triangle FEQ_3, having two vertices at the same height (E and F) and the third vertex Q_3 at the height of a contiguous contour line. The skeleton of the region EQ_aF is the polyline Q_aQ_2, where Q_a is a DAP. The skeletal points, Sk_k, of the polyline $Q_aQ_2Q_3$ are assigned height values according to the formula

$$z_{Sk_k} = \frac{x_{Sk_k} z_{Q_3} + (L - x_{Sk_k}) z_{Q_a}}{L}, \quad (1)$$

where x_{Sk_k} is the coordinate along the polyline $Q_aQ_2Q_3$ with origin in point Q_a; L is the total length of the polyline $Q_aQ_2Q_3$; and z_{Sk_k}, z_{Q_a}, z_{Q_3} are the heights of points Sk_k, Q_a, and Q_3, respectively.

[21] If the contour line is a closed line with no other internal features (contour lines or isolated spot heights), the internal IB is heighted by assigning to the skeletal point, at middle distance along the IB, the height value equal to $z_{Q_a} \pm \Delta z/2$, where Δz is a given maximum interval (for example, the difference in elevation between the two contiguous contour lines). The sign depends if it is a hill or a hollow.

[22] In conclusion, we propose the algorithm DEST. Given a set of isolated spot heights and segments discretizing contour lines, a CDT is performed. The principal skeletons of the flat regions created by the CDT are computed and assigned heights. A new CDT is then performed, considering all the isolated spot heights, the segments approximating the contour lines, and the segments of the computed (3-D) principal skeleton. In such a way the gullies and the ridges computed by DEST become sides of the triangles of the TIN. The new 3-D network of triangles in space does not contain the artifacts typical of a traditional DT of contour line curves.

4. Comparison of DEST With Other Algorithms

[23] The DEST algorithm has been compared with other techniques, selecting for this purpose four algorithms most commonly used of the many available in the literature. They belong to the three main groups proposed by *Watson* [1992]: distance-based methods (inverse-distance-based gradients), triangle-based methods, and neighborhood methods. Many of them are also implemented in commercial software.

4.1. Method A

[24] This approach was suggested by Eastman and coworkers [*Eastman et al.*, 1993; *Eastman*, 1995]. For each mesh point the intersections of the principal axes and their bisectors with nearby contour lines are evaluated and are used to compute the interpolated heights and slopes. The height associated with the maximum slope is then chosen at the mesh point height.

4.2. Method B

[25] This technique is based on the approach by Borgerfors [*Gorte and Koolhoven*, 1990]. The minimum distances of each contour line from the interpolation point are evaluated. A linear interpolation is then performed using the two distance values and the two nearest contour values.

4.3. Method C

[26] This approach is based on a constrained Delaunay triangulation of the contour lines. This method is implemented in the ERSI products.

4.4. Method D

[27] In this approach the CDT of the contour lines is evaluated. In the flat areas computed by the CDT, some inferred breaklines are evaluated as the lines joining the medial points of the internal sides of the flat triangles. This IB is linearly heighted according to the contiguous contour line values, along its path. This approach is implemented in the MGE INTERGRAPH software.

4.5. Method DEST: The Algorithm Proposed in This Paper

[28] The CDT of the contour lines is evaluated. In the flat areas computed by the CDT, inferred breaklines are evaluated as the principal skeleton of the flat terraces.

[29] According to *Watson*'s [1992] classification, algorithms A and B belong to the distance- and neighborhood-based methods, whereas methods C, D, and DEST are triangle-based methods.

[30] Other methods produce effects that are easily quantifiable. Since points are structured along contour lines, a DEM evaluated by a Kriging technique, considering an area of influence around the interpolation point, presents contour line ghost effects [*Armienti and Pareschi*, 1987; *Barberi et al.*, 1992]. DEM generation based on contour line dilatation is influenced by the vector-to-pixel approximation used in the dilatation procedure [*Taud et al.*, 1999]. Since the input points for the interpolation are chosen along predefined directions, distance-based methods produce DEMs with

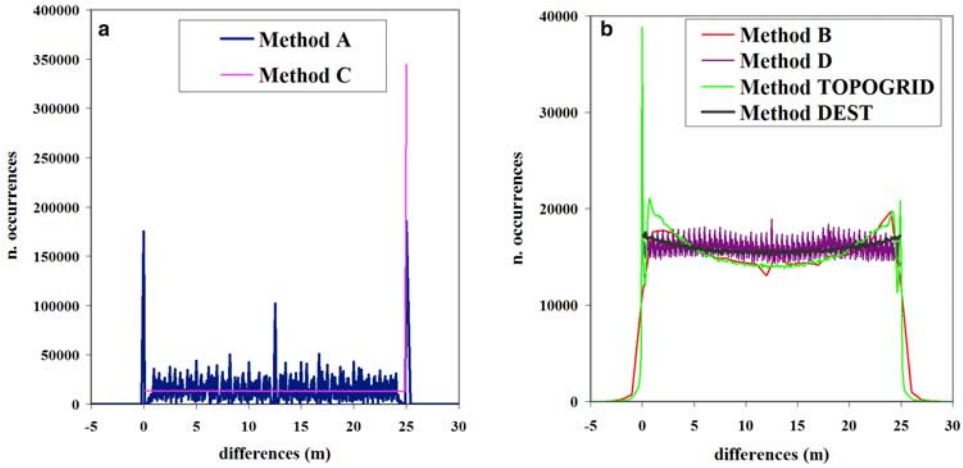

Figure 7. Number of occurrences versus the differences between grid z value and the lower contour line height (the pair of contiguous contour lines enclosing the grid point is considered). The test area is 10 × 10 km wide, with a contour line interval of 25 m. (a) Methods A and C; (b) methods B, D, TOPOGRID, and DEST. Methods A, C, and TOPOGRID show marked peaks in correspondence of the two boundary values 0 m and 25 m. Near these two boundary values, TOPOGRID shows sink values too. Methods B and TOPOGRID do not satisfy criterion 2, i.e., the DEM elevations do not range inside the isohypse equidistance. For less then 1% of DEM points, method DEST retains small overestimations/underestimations related to contour levels.

artificial structures along these directions. Other sophisticated methods are not considered here since they are unable to fully benefit from the organization of the input points as contour lines. In the following section a specific comparison is done between DEST and the TOPOGRID algorithm [*Hutchinson*, 1989], one of the most diffuse worldwide approaches.

[31] Methods A, B, C, and D, TOPOGRID, and the DEST method have been tested on a 10 × 10 km site in the Campania region of southern Italy. The contour lines of a portion of this square site are shown in Figure 12. The DEMs used for comparison have a 10 m resolution step. The input vector data are isohypses derived from a 1:25,000 map, UTM ED50.

[32] Different techniques can be adopted to evaluate the performance of interpolation algorithms [*Carrara et al.*, 1997; *Hutchinson*, 1989; *Wood and Fisher*, 1993; *Liu and Jezek*, 1999]. The following criteria have been used in the validation of methods A to D and DEST: (1) DEM points falling along a contour line must have the same elevation as the isohypse; (2) the DEM elevations must fall within the isohypse equidistance range between two contiguous contour lines at different quotes; (3) the vertical distance of DEM elevation from the nearest lower contour line has a rectangular distribution, reflecting no tendency of the interpolated data to cluster preferentially around nearby contour quotes; and (4) no bias must be present in the distribution of aspects.

[33] All the methods A–D and DEST satisfy criterion 1. Criteria 2 and 3 have been verified by the height distributions between all the pairs of contiguous contour lines, referred to the lower contour line height. The contour line interval of the test site is 25 m so that all the differences are expected to fall in the range 0–25 m. A rectangular distribution (elevations that are uniformly distributed) occurs if no bias effects are present in the DEM [*Reichenbach et al.*, 1993]. In all the DEMs, except for those created using methods D and DEST, the distributions of relative elevation differences present two major bias peaks (0 m and 25 m) (Figures 7a and 7b): that is, all these algorithms reconstruct false flat morphologies at contour heights. The phenomenon increases as the DEM resolution increases [*Wood and Fisher*, 1993].

[34] Method D can overestimate (underestimate) heights in convex (concave) regions, depending on the point distribution along contour lines. In fact, the inferred breaklines of method D connect the medial points of the internal triangle sides. These lines display abrupt changes in direction and, near the lower (higher) contour line, the first medial point has a higher (lower) value than expected (because of its closeness to the isohypse). In conclusion, the inferred breaklines of method D, because they are heighted along their path, introduce anomalous hills or sinks.

[35] The distribution of aspects is evaluated for all the methods (Figure 8). Methods A, B, and C produce horizontally flat regions, for which an aspect angle is not defined. In the present test case the percentage of these areas is 3.7%, 2.4%, and 18.6% for methods A, B, and C, respectively. Methods A, B, and D have anomalous peaks in the aspect distribution in correspondence to the "natural" angles of a square mesh: $\pm\alpha_i$, $90 \pm \alpha_i$, $180 \pm \alpha_i$, and $270 \pm \alpha_i$, with $\alpha_i = \arctan(n/m)$, n and $m \in \mathbf{N}$, with $n < m$. The most pronounced peaks occur at $0° + n\ 45°$, $n \in \mathbf{N}$. In contrast, the DEST algorithm shows no such artefacts.

5. Comparison of DEST With TOPOGRID

[36] One of the most common algorithms used to evaluate DEMs from contour lines is TOPOGRID [*Hutchinson*, 1989]. It is based on an interpolation approach that derives quotes on a regular grid by minimizing a discretized invariant roughness penalty defined in terms of first- and

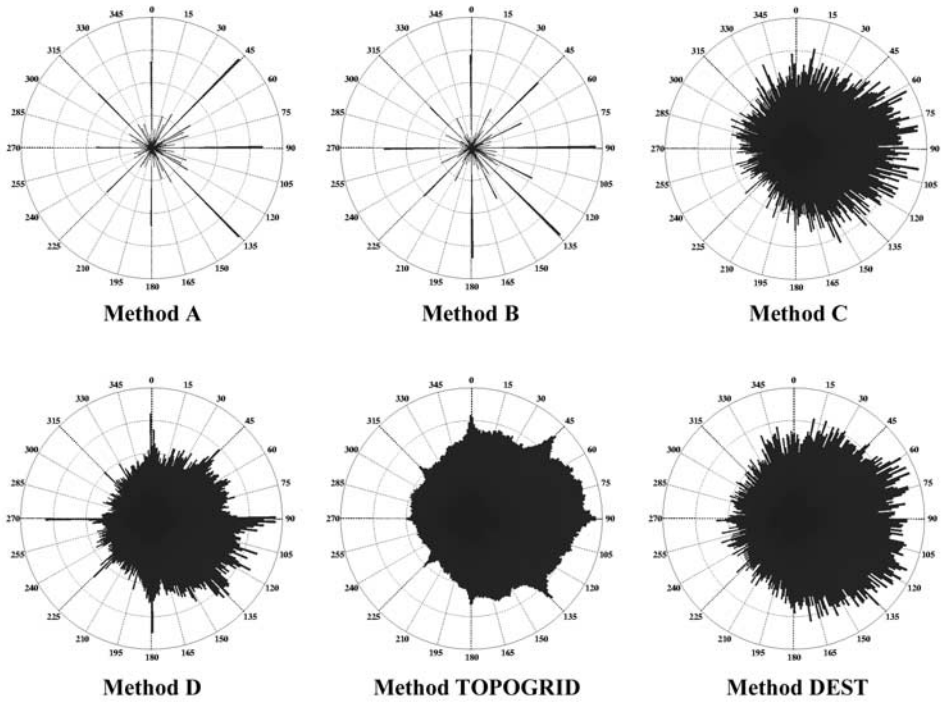

Figure 8. Angular distributions of the aspects for each method for the test site (see Figure 12). Horizontal (flat) areas introduced by methods A, B, and C are not represented in the diagrams. Methods A, B, and TOPOGRID show anomalous peaks in the aspect distribution connected with the "natural" angles of a square mesh ($0° + n\,45°$, $n \in \mathbf{N}$). Method D shows anomalous peaks mainly at 0°, 90°, 180°, and 270°.

second-order partial derivatives of the fitted function. The iteration technique utilizes a simple nested grid strategy that calculates grids at successive finer resolutions, starting from an initial coarse grid, and successively halving the grid spacing until the final user-specified grid resolution is obtained. The interpolation technique introduces spurious pits and sinks. To avoid these spurious effects, *Hutchinson* [1989] introduces a drainage enforcement algorithm that removes, within tolerances specified by the user, the pits and sinks along the drainage paths.

[37] TOPOGRID has been tested on a 10 × 10 km site, located in the Campania region, southern Italy. Grid step is 10 m. Part of the text area is shown in Figure 12. As depicted in Figure 7b, the DEM elevation between two contiguous contour lines at different quotes do not fall within the isohypse equidistance range (some values are, in fact, lower than 0 m and greater than 25 m). The vertical distance of DEM elevations from the nearest lower contour line also show anomalous values at and near zero (i.e., peaks and sinks near contour line z values) (Figure 7b).

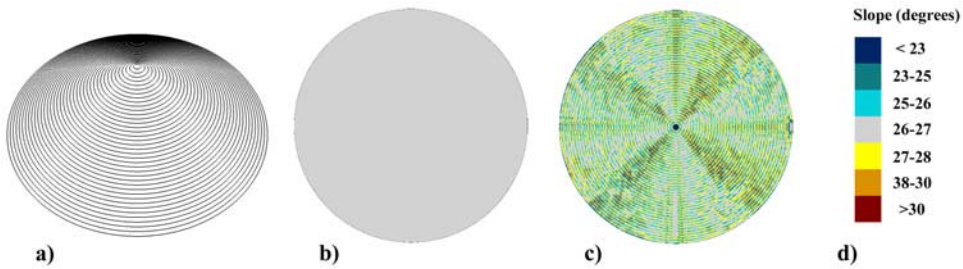

Figure 9. (a) 3-D view of equispaced contour lines of an ideal cone, with constant slopes (26.5°). If r_0 is the radius of the cone base, the contour line interval is 0.013 r_0, and the cone height is $r_0/2$. (b) Slopes of the TIN-based cone reconstructed by DEST. The uniform gray level values indicate a nearly constant slope according to the slope color table in Figure 9d. (c) Slopes of the cone reconstructed by TOPOGRID. Ghost effects (radial noise), related to contour lines, are present, indicating a stepped cone; further, more pronounced noise occurs along preferred directions ($0° + n\,45°$, $n \in \mathbf{N}$) related to the grid-based interpolation of TOPOGRID.

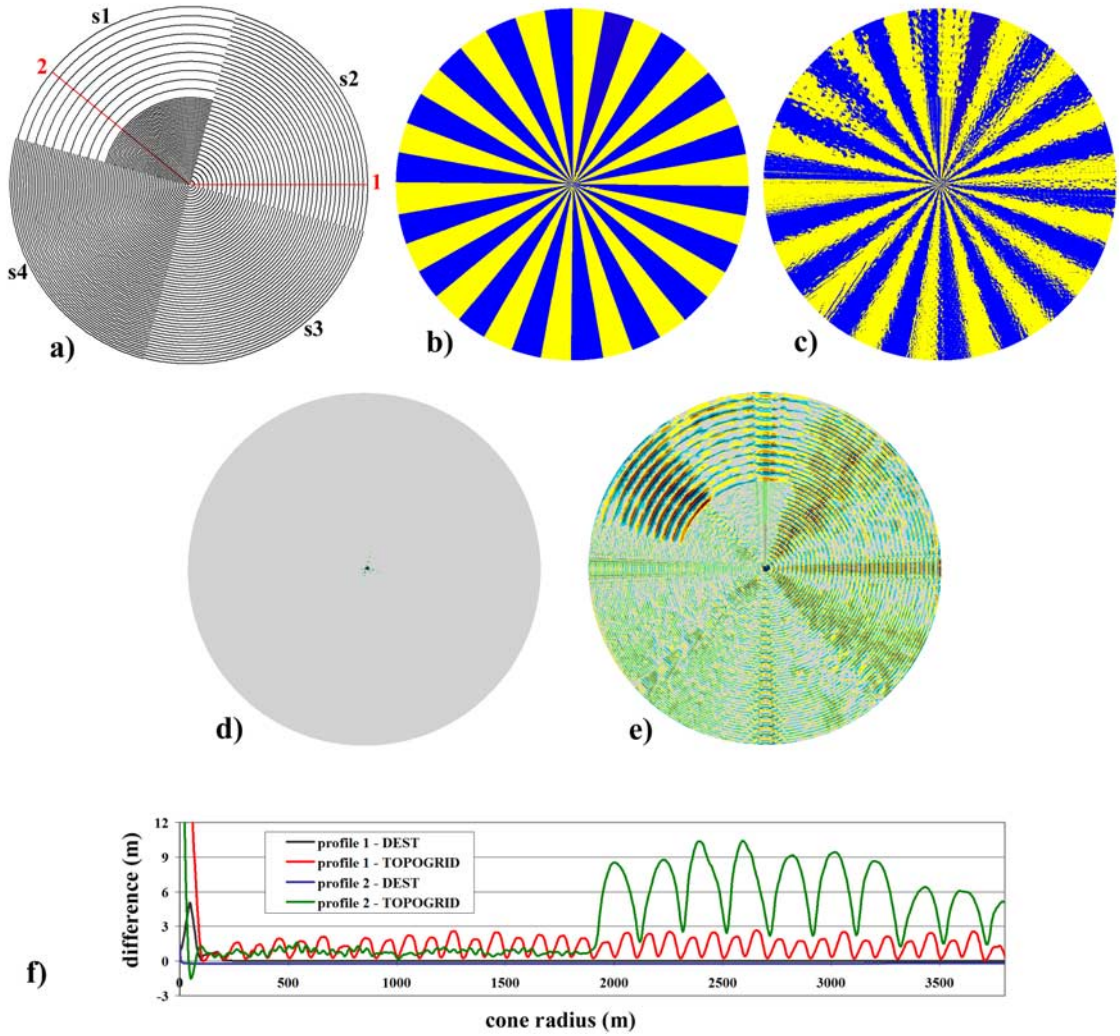

Figure 10. (a) An ideal cone with constant slopes (26.5°) is sketched by contour lines at varying intervals. If r_0 is the radius of the cone, the cone height is $r_0/2$. In region s1 the contour line interval is 0.005 r_0 (internal region) and 0.026 r_0 (external region), respectively; in region s2 the contour line interval is 0.013 r_0; in region s3 the contour line interval is 0.0085 r_0, and in region s4 the contour line interval is 0.006 r_0. (b) Aspects of the cone reconstructed by DEST (similar to the ideal ones). Different aspects are grouped in 10°-sized intervals, represented with two alternate colors. (c) Aspects of the cone reconstructed by TOPOGRID. Noise is present, with a pattern dependent on the contour line interval. (d) Slopes of the cone reconstructed by DEST. The almost uniform gray level values indicate a nearly constant slope. (e) Slopes of the cone reconstructed by TOPOGRID. Noise effects related to contour lines are present. In both Figures 10d and 10e the slope color table is that of Figure 9d. (f) Differences between the ideal cone directrix and the surface reconstructed by TOPOGRID and DEST along profiles 1 and 2. The differences present a discrepancy with a frequency equal to the contour line intervals in the case of TOPOGRID.

[38] The distribution of aspect also shows anomalous values, at $0° + n\ 45°$, $n \in \mathbf{N}$, related to the square mesh structure of the roughness penalty minimization performed by TOPOGRID (Figure 8). Additionally, the angular distribution of aspects in TOPOGRID is smoothed: the drainage enforcement algorithm of TOPOGRID tends to remove not only spurious sinks but also, in part, natural features with characteristic dimensions below the tolerances of TOPOGRID.

[39] The artefacts related to the ghost effects of contour lines and anomalous preferred aspects can easily be detected on an analytical surface that does not present the roughness (masking) effects of a natural landscape. A conical surface was chosen for the test (Figure 9), where the source consists of equispaced contour lines with a constant slope of 26.5°. Since here no drainage paths are present, no spurious sinks are introduced by TOPOGRID and it is possible to test the efficiency of the minimization algorithm of TOPOGRID. The noise introduced by the minimization of the roughness penalty, clearly visible in the slope image (Figure 9c), has a frequency that is related to the contour line interval.

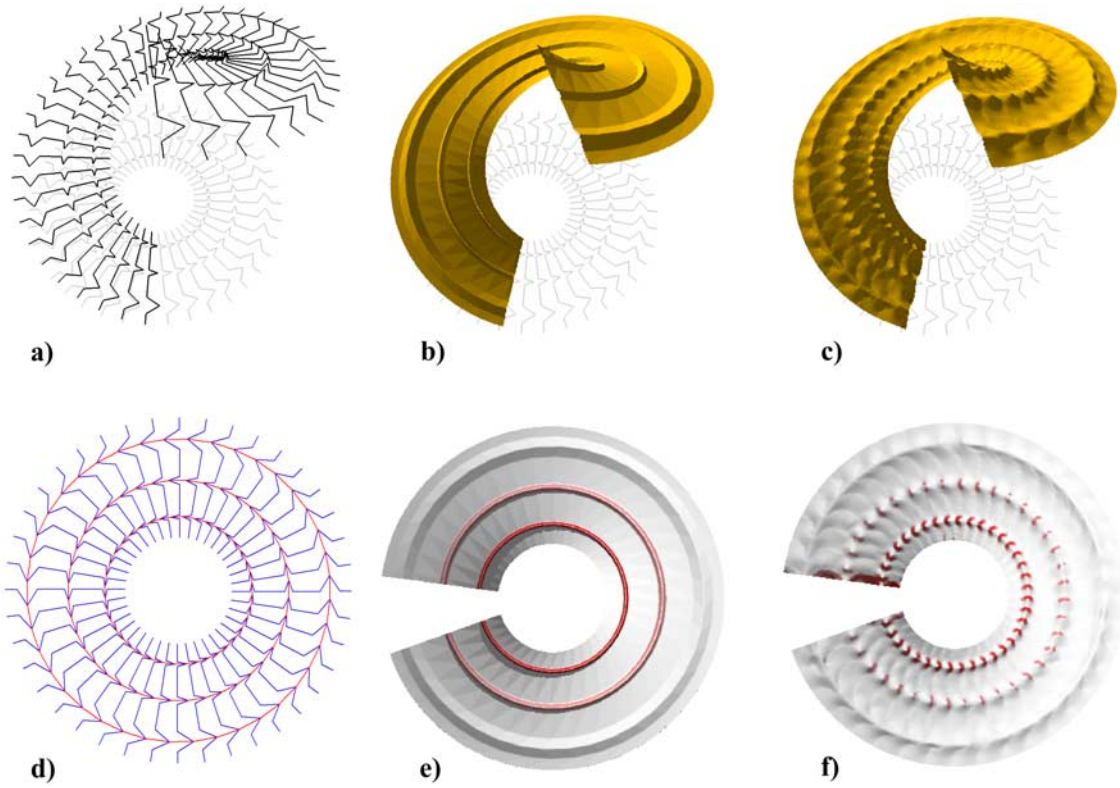

Figure 11. (a) Perspective view and projection in the horizontal plane of contour lines along a helicoidal belt with three parallel ridges. (b) Reconstruction of the belt by the DEST algorithm. (c) Reconstruction by TOPOGRID. Tolerances used are the recommended ones, while the number of iteration is 30. (d) Breaklines computed by DEST (red lines) coinciding with the real ridges. (e) Correct slopes reconstructed by DEST (red means slopes greater than 50°). (f) Slopes of the grid reconstructed by TOPOGRID showing pronounced artifacts, with a density increasing toward the internal edge of the elicoidal belt.

[40] In general, the contour lines show variations in their average density, e.g., in areas passing from steep slopes to flattish zones, where there is a slope break or where contour lines coming from different sources may be at different resolution. The behavior of DEST and TOPOGRID has been investigated in these regions. A cone with a constant slope (26.5°) is reconstructed by contour lines having a density that varies with the sector (Figure 10). Within a sector, there is a change in contour line density, depending on contour line radius. There are no particular effects either in TOPOGRID and DEST reconstruction at the boundaries between regions with different contour line densities. However, as in the example shown in Figure 9, slopes reconstructed by TOPOGRID generally show noise, whose frequency depends on the contour line spacing (Figures 10e and 10f), with an increase along the square mesh preferred directions mentioned above ($0° + n\ 45°$, $n \in \mathbf{N}$).

[41] Furthermore, noise introduced by TOPOGRID could have a no-zero mean, showing a systematic trend as shown in Figure 10f (positive values of the differences, i.e., overestimated heights). This overestimation occurs also for the Vesuvius volcano cone (average value of the discrepancy = 0.3 m for the Vesuvian area of Figure 16 (inside the line). These no-zero mean discrepancies could involve errors in volumes estimated by TOPOGRID.

[42] Also, aspect exhibits a noise pattern that depends on contour line density (Figure 10c). No artefacts are present in the cone reconstructed with DEST (Figures 10b, 10d, and 10f), except for discretization effects at the top of the cone.

[43] A crucial point in TOPOGRID is the removal of pits and sinks introduced by the minimization of the invariant roughness penalty. Since removal is achieved along ridges and drainage, the "reliability" of the interpolated values strongly depends on the ability of the drainage enforcement algorithm of TOPOGRID to evaluate these morphological features. Removal can sometimes fail, for two main reasons: (1) TOPOGRID is not always able to detect the correct drainage network and (2) the tolerances introduced by TOPOGRID for further removal of sinks and pits are the same throughout the domain so that they cannot adjust to changes in contour line density. Figure 11 shows an ideal helicoidal belt. Given the internal radius r_0, the external radius is 3.33 r_0, the difference between the minimum and maximum contour line height is 6.5 r_0, and the contour line interval is 0.17 r_0. Along the belt are three ridges running parallel to each other. Near the internal side of the belt, the distance between points along the same contour line (located where the contour lines change direction) is similar

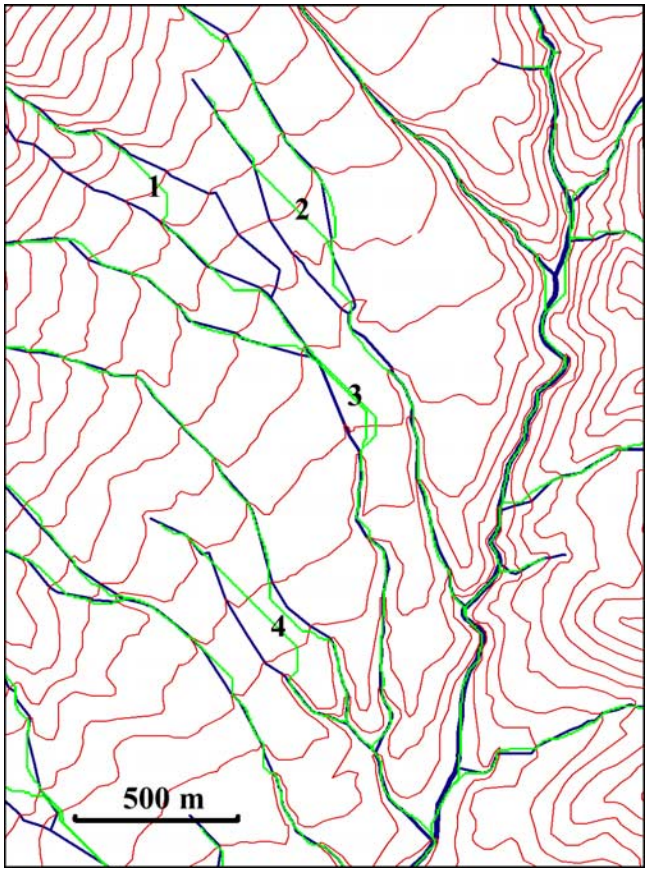

Figure 12. Contour lines (red) of a natural landscape. The contour line interval is 25 m. Green lines are the drainage computed by TOPOGRID, and blue lines are the drainage (breaklines-based) computed by D-DEST. As can be simply verified in points 1, 2, 3, and 4, TOPOGRID is not always able to correctly identify the drainage paths, and "jumps" of the drainage path can occur from one gully to the next nearest gully, across weak ridges.

to the distance between contiguous contour lines. Along the internal side of the belt, TOPOGRID is unable to adequately reconstruct ridges because the similar distances between points of the same contour line and points of nearby lines. Increasing the value of the tolerances and the number of iterations of TOPOGRID by 300%, with respect to the default recommended values, does not bring any improvement. In the TOPOGRID reconstruction, similar effects occur if gullies (instead of ridges) are introduced in the contour lines of the helicoidal belt of Figure 11. On the contrary, DEST does not introduce any artefact. Figure 11e shows that our algorithm is insensitive to the digital sampling interval along the contour lines (from the internal edge of the belt to the external one, in the contour lines of Figure 11a, this interval increases; points are, in fact, located at the change of direction of contour lines).

[44] The contour lines of a natural landscape are shown in Figure 12. Again, no sinks are removed where TOPOGRID does not clearly identify drainage. As shown in Figure 12, in the TOPOGRID surface reconstruction, jumps of the drainage path can occur from one gully to the next nearest gully, across weak ridges. As a result, there is no local elimination of artificial sinks and erroneous drainage identification and inaccurate estimates of the catchment areas.

6. Drainage Path and Catchment Areas From DEST

[45] Topography plays an important role in the distribution and flux of water and energy within natural landscapes. Drainage and related features such as ridges, valley bottoms, channel networks, and surface drainage patterns can be simply derived by a raster DEM, with grid elevations at a regular mesh. The D-8 method [*Fairfield and Leymarie*, 1991] is one of the most diffuse ones. This approach identifies the steepest downslope flow path between each cell of a raster DEM and its eight neighbors (hence the name D-8 method) and defines this path as the only flow path leaving the raster cell. The drainage network is identified by selecting a threshold catchment area, at the bottom of which a source channel originates; all cells with a catchment area greater than this threshold catchment area are classified as part of the drainage network. This drainage network identification approach is simple and directly generates connected networks [*Martz and Garbrecht*, 1995]. Channel and drainage area capturing occurs when the DEM resolution can no longer resolve the separation between channels or drainage boundaries. In such situations the number of channels, the size of direct drainage areas, and the channel network pattern depend on grid resolution and may depart considerably from the real ones [*Martz and Garbrecht*, 1995]. The use of the D-8 method for catchment area and drainage network analysis has been further criticized by different authors on the grounds [*Quinn et al.*, 1991; *Costa-Cabral and Burges*, 1994]. For example, anisotropy introduced by the use of regular grids fails to represent adequately divergent flow over convex slopes and can lead to a bias in flow path orientation [*O'Callaghan and Mark*, 1984; *Fairfield and Leymarie*, 1991]. Many techniques have been proposed to solve this problem, among them the use of a multiple flow instead of the single flow direction away from a DEM cell [*Quinn et al.*, 1991]. However, although the multiple flow direction algorithm seems to give superior results in the headwater region of a source channel (overland), a single flow direction algorithm is superior in zones of convergent flow and along well-defined valleys [*Freeman*, 1991; *Quinn et al.*, 1991].

[46] All the above described problems are related to the grid structure, which, for its regular mesh organization, does not adjust to variations in terrain feature density (steep slopes, gullies, ridges, flat areas, etc.). On the other hand, TINs allow for variable spatial resolution, and they generally consist of a simple organization of the input data (triangles) by adding topological connection. With the introduction of ridges and valleys the DEST triangulation guarantees that gullies and ridges (added breaklines) be sides of the triangular network discritizing the terrain surface.

[47] We suggest a simple but efficacious technique to evaluate the drainage path in a TIN-based digital elevation model, named D(rain)-DEST. At each triangle node (instead of at the grid node of the D-8 method) the D-DEST algorithm we suggest identifies the steepest downslope flow

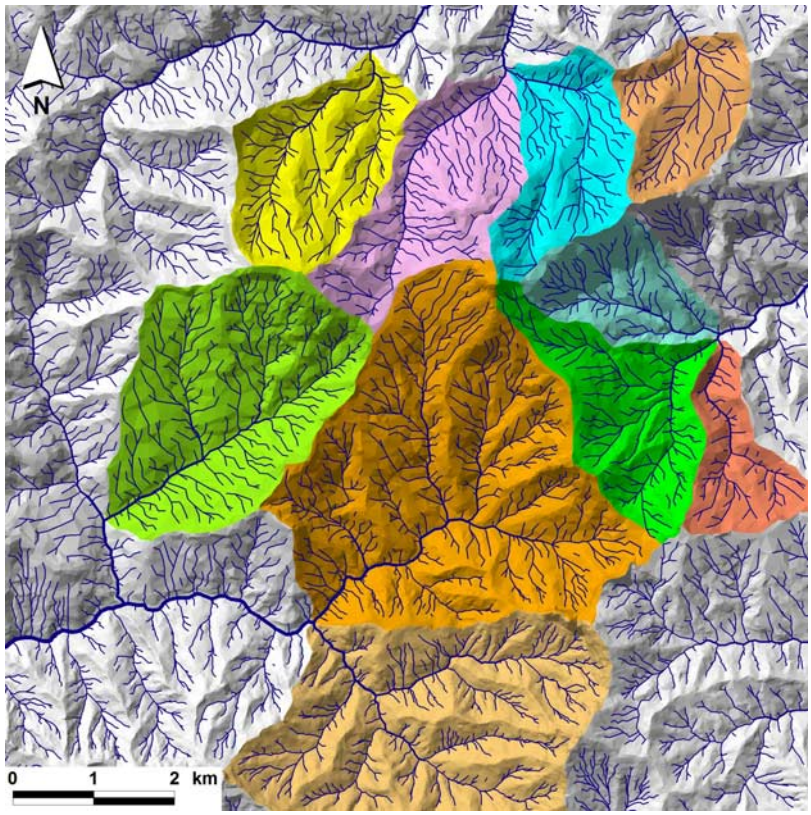

Figure 13. Drainage network and catchments areas computed by D-DEST: the thickness of the drainage paths depends on the catchment area.

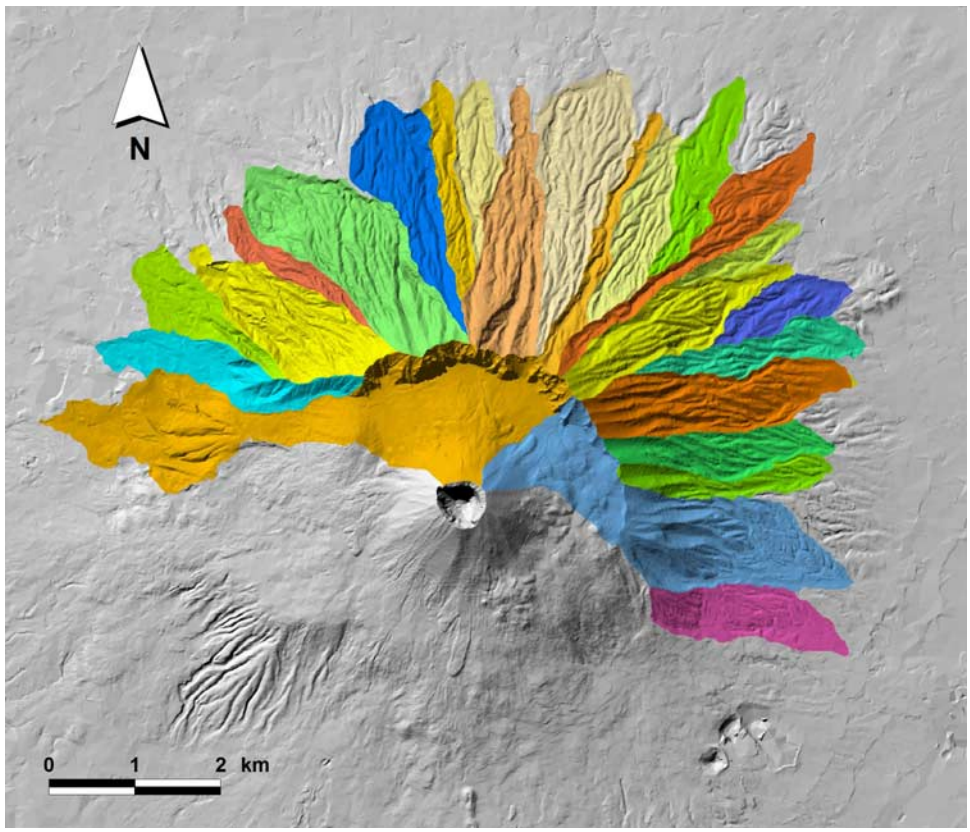

Figure 14. Basins of the northern flanks of Vesuvius volcano (southern Italy), computed by D-DEST.

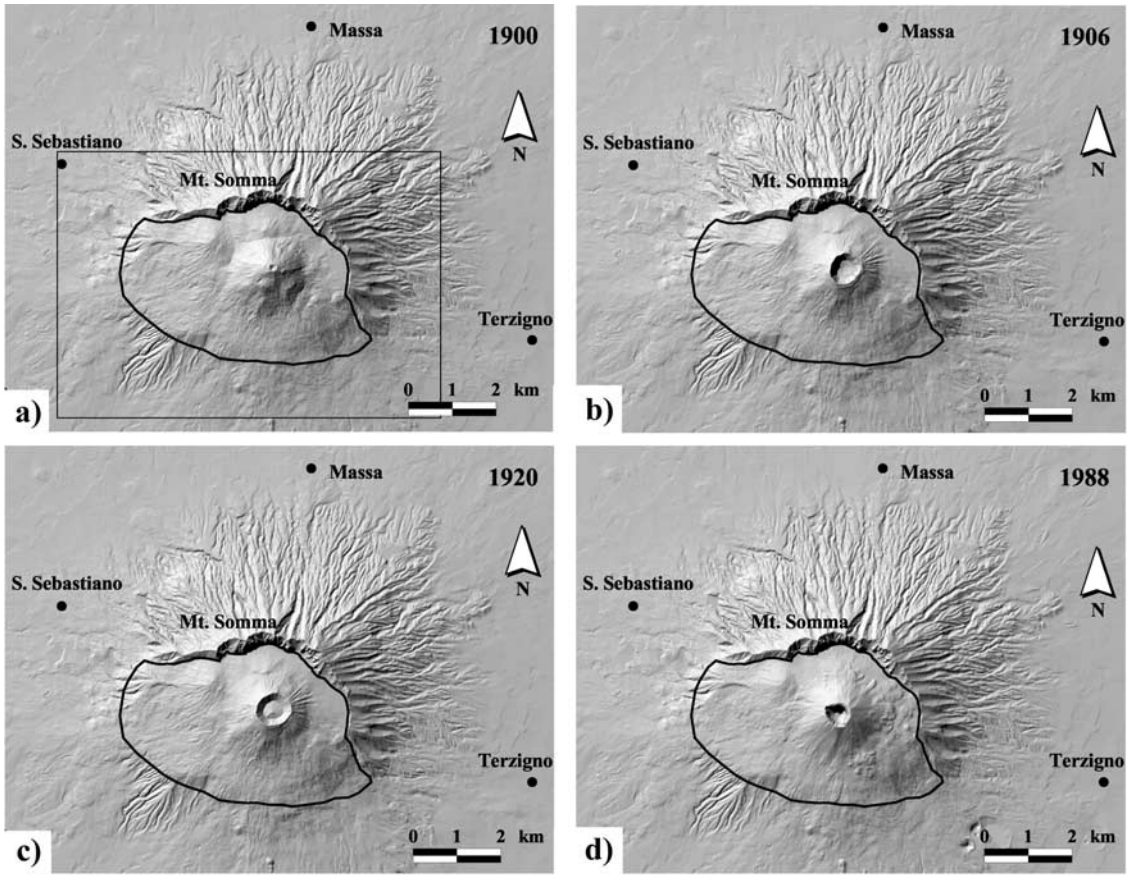

Figure 15. Cone morphology of Vesuvius in (a) 1900, (b) 1906, (c) 1920, and (d) 1988, as reconstructed by the DEST algorithm. The box in Figure 15a is the area covered by Figure 16. The coordinates of the bottom left corner are (UTMED50) longitude 445634E; latitude 4515646 N.

path among all the triangle sides departing from that node and defines this path as the only flow path leaving the node. The drainage network is identified by selecting a threshold catchment area, at the bottom of which a source channel originates; all triangle sides with a catchment area greater than this threshold catchment area are classified as part of the drainage network. The catchment area of the single triangle is assigned to one or more nodes (vertexes), depending on the local triangle gradient. This approach is simple and directly generates connected networks, permitting the exact delineation of catchment areas and drainage on very large areas almost in very short times (<1 s on a PC for the tile 10 $\times$ 10 km of Figure 11), keeping everywhere the resolution of the input data. The fastness of the technique (up-down to compute the drainage catchments, and down-up to identify a basin) depends on the tree structure of the computed data. It is important to remark that all the gullies identified by the DEST algorithm belong to the drainage network of D-DEST. An example of the drainage network computed by D-DEST is reported in Figure 12 (only the drainage paths with a catchment area greater than a given threshold (in Figure 12, 120,000 m^2) are reported). In Figure 13 an example of the drainage network and of some basins (catchment areas greater than a fixed threshold, 10000 m^2 in the figure) computed by D-DEST is reported. The considered area is a portion of the above-mentioned 10 $\times$ 10 km site in the Campania region. The same approach has been applied to evaluate the basins of a central cone morphology too, like the Vesuvius volcano. The identification of these basins allows, for example, a better zonation of hazard related to debris flow developing on Vesuvius slopes in case of eruption. In the northern sector of Vesuvius cone (Figure 14), differences in basin areas identified by D-DEST and TOPOGRID (10 m grid) range up to 10%.

7. An Application: The Reconstruction of Vesuvius Volcano

[48] As a typical application of the DEST algorithm, we reconstructed the evolution of the Vesuvius volcanic cone (Campania region, southern Italy) in the twentieth century, using historical maps. The input topographic data are contour lines and spot heights, used by DEST to create the TIN of the area.

[49] The conical shape of Vesuvius volcano is a result of the accumulation of products from the central vent during explosive and effusive eruptions. In the last 20 centuries [*Cioni et al.*, 1999] the Vesuvian cone has evolved within the caldera of an older volcano, Mt. Somma, which is clearly visible in the northern sector (Mt. Somma ridge, Figures 15 and 16). During the last century the main eruptions occurred in 1906 and 1944 [*Arrighi et al.*, 2001]. The 1906 eruption started in May 1905 with slow lava effusions and intermittent strombolian activity. In April

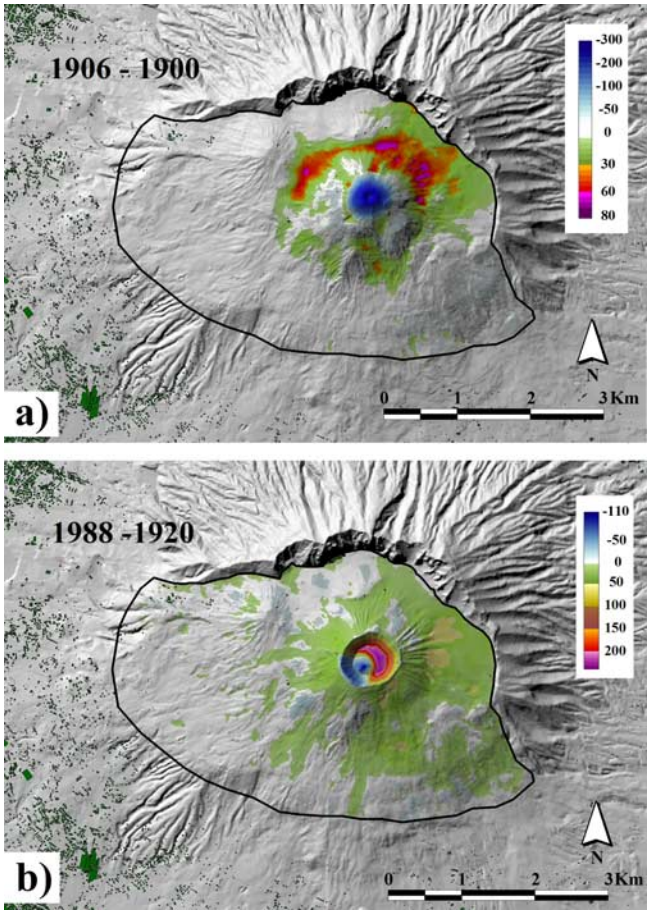

Figure 16. Differences in elevation (in meters) due to eruptive deposition superimposed to the previous morphology: (a) differences 1906–1900 and (b) 1988–1920. The line defines the area within which volume differences computations were made.

1906 the eruption reached a climax with lava fountains and earthquakes. The top of Vesuvius was truncated, and a vast crater developed; an eruptive column of ash and gases reached a height of 13 km. The eruption ended at the end of April. After a short period of quiescence, Vesuvius was again characterized by permanent activity from 1913, with the quiet effusion of lava and minor explosions from a small conelet slowly filling the crater left by the 1906 eruption. In 1929 a major lava flow overflowed from the Somma caldera rim and reached the village of Terzigno, on the eastern slopes of the volcano, followed by lava fountains and seismic tremors. By 1944, the 1906 crater had almost filled. The 1944 eruption was characterized by lava flows (invading the villages of Massa and S. Sebastiano), lava fountains, a sustained ash plume, small pyroclastic flows, and lahars. The 1944 event was the last one, and since then, the volcano has been quiescent, with no major signs of activity [*Rosi et al.*, 1987; *Arrighi et al.*, 2001].

[50] The upper cone variations of Vesuvius have been reconstructed by the DEST algorithm applied to topographic data from the following historical maps: (1) the Istituto Geografico Militare Italiano (IGM) survey of 1900, with corrections in 1904; (2) the IGM survey of 1906; (3) the IGM survey of 1920; and (4) the survey of 1988, integrated with that of 2001 [*Pareschi et al.*, 2000a, 2000b, 2002].

[51] The altimetric errors on the 1900/06/20 and 1988 maps are ±1.5 m (90% of cases) and ±0.6 m (90% of cases), respectively. Figures 15a–15d show the upper cone morphology in 1900, 1906, 1920, and 1988/2000, as reconstructed by the DEST algorithm. The morphological changes have been updated only inside the dark line, in the range 750–800 m above sea level (asl). Outside the line, the topography is the last available one. Figures 16a and 16b illustrate the differences in elevation caused by an eruption superimposed on the preceding morphology (differences 1900–1906 and 1920–1988). During the 1906 eruption the preceding cone was truncated and eroded, taking on the shape of a funnel. From the reconstructed TINs the maximum and minimum crater rim heights pass from 1335 m and 1285 m asl to 1220 m and 1120 m, respectively, and the bottom of the crater from 1240 m to 985 m. The volume removed from the crater during the 1906 eruption is estimated to be 67 million m^3 (compare 84 million m^3 heuristically evaluated by *Nazzaro* [1997]). On the slopes of the upper cone (inside the closed line of Figures 16a and 16b), the volume increase in the period 1900–1906 is 105 million m^3, mostly from lava flows, tephra fallout, and ballistics.

[52] The 1944 eruption changed the morphology of the upper cone again. The 1906 vent, filled in the period 1906–1944 by intermittent activity, is modified again during the 1944 event. The volume increase on the upper flanks is 175 million m^3, again as a result of lava flows, tephra fallout, and ballistics.

8. Conclusions

[53] An improved method (DEST) is described for generating TINs from contour lines and spot heights. It is well known that a Delaunay triangulation or a constrained Delaunay triangulation introduces false morphological features (flattened terraces), especially in areas where the contour lines display high curvature. Many attempts have been made to avoid the ghost effects related to the nonrandom distribution of input contour line points. The DEST method reconstructs the principal skeleton of morphologically anomalous flattish areas introduced by a CDT. From these, new inferred breaklines are used as additional segments in the modified CDT. The method could be applied to historical maps, where the elevation information is confined to contour lines only, and in general to existing topographies acquired through isohypses.

[54] The main advantages presented by DEST compared with other algorithms from literature, i.e., TOPOGRID, are as follows.

[55] 1. There are no constraints on the digital sampling intervals along contour lines (see Figure 11e where, from the internal edge of the belt to the external one, this interval increases without problems).

[56] 2. There is a simple format of the input data: just isolated spot heights and contour lines (as polylines).

[57] 3. No arbitrary (i.e., chosen by a user) tolerances have to be specified, as, for example, in TOPOGRID.

[58] 4. There are facilities for processing input data at different resolutions and from different sources, without bias effects. For example, Figure 17 shows the TIN recon-

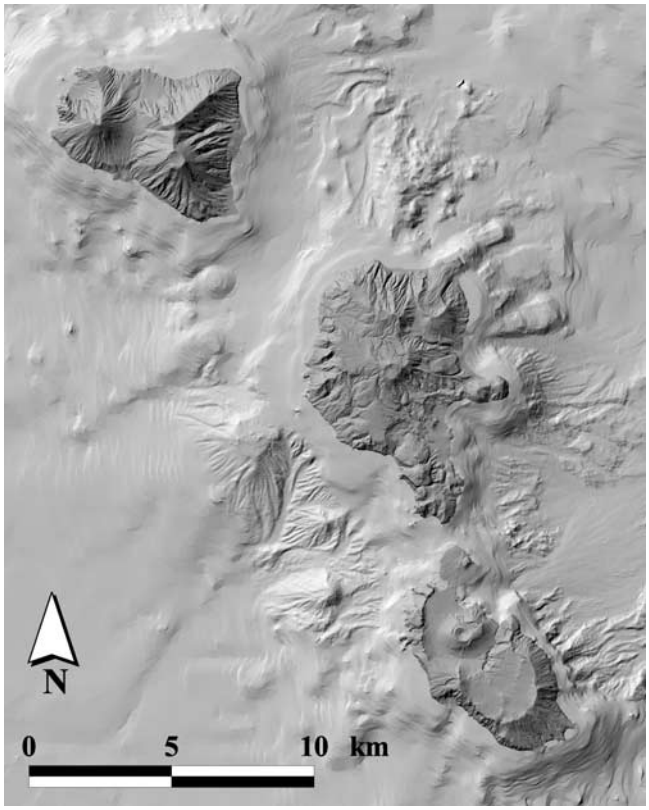

Figure 17. TIN, computed by DEST, of the Aeolian Islands (from bottom to top: Vulcano, Lipari, Salina Islands), southern Tyrrhenian Sea, north of Sicily.

structed by DEST for the Aeolian Islands. For land, input data are spot heights and contour lines from 1:10,000 maps; the La Fossa Cone of Vulcano Island (bottom left in Figure 17) comes from a digital photogrammetric grid, 1 m resolution [*Achilli et al.*, 1998]; for the sea bottom, data are from monobeam and multibeam echosounders along radial paths around the islands [*Bisson et al.*, 2003].

[59] 5. There are no bias effects in slopes and aspects. This is an important characteristic for geomorphological applications but also in other fields. In SAR data processing, for example, an "external" DEM supports the integration of height information in the areas affected by shadowing, layover, or lack of coherence in SAR data. A digital terrain model without bias effects in slopes and aspects guarantees the generation of homogeneous and seamless final data.

[60] 6. DEST has the capability to compute ridges and gullies and, as a consequence, drainage paths and catchment areas. Since these morphological features are based on a TIN structure, no biased directions occur.

[61] 7. DEST has the ability to also detect shallow incised valleys on very gentle slopes and weak ridges (Figures 11 and 12).

[62] 8. DEST has the capability to work with a large number of data. For example, for the Sicily region, southern Italy, 25,708 km^2, a total number of 9.7 million input points have been used by DEST to reconstruct the TIN; 8.5 million points were added along the principal skeletons and 35 million triangles created by DEST.

[63] 9. DEST has been extensively tested on many million of points without problems (see the above-mentioned example of Sicily, for example).

[64] 10. Computational times are very short, one third of TOPOGRID in the case of the 10 $\times$ 10 km test area mentioned in the text (with a 10 m grid step). The time doubles with respect to an ordinary DT/CDT.

Appendix A: Skeleton Reconstruction by DEST

[65] The medial axis of a set of distinct points of the plane (number >2) is the boundary of the Voronoi diagram of all the points so that the medial axis is a generalization of the Voronoi diagram. Some useful properties of medial axes are as follows: (1) the medial axis of a set of linear segments consists only of straight lines and parabolic arcs; (2) the skeleton of a convex polygon consists only of linear segments; (3) the skeleton of a simply connected region (i.e., without holes) is a tree (in the graphical theoretical sense); (4) if Q is a point of the boundary B of a plane set R, where the curvature of B has an isolated maximum, then there exists a branch of the skeleton of R terminating at Q; (5) the medial axis of a straight line r and a point P not belonging to r, is the parabola with directrix r and focus in P; (6) the medial axis of two incident straight lines is given by the two bisecting lines; and (7) the medial axis of a circumference is a single point: its center.

[66] Let us consider the generic flat region created by a DT, for example, where an isohypse presents a high curvature. Locally, this isohypse is approximated by N_s contiguous segments connecting N_p points. This flat region is constituted by a set of flat triangles with vertices in N_p. The computation of the skeleton of this region is essentially a problem of determining in the plane the skeleton of the set S (N_p, N_s), constituted of N_p segments and N_p points. Let T_1 be the set given by the union of all the bisectors of all the pairs of straight lines on which the N_s segments lie; let T_2 be the set given by the union of all the axes of all the segments with end points in the N_p points; let T_3 be the set given by the union of all the parabolas that can be constructed taking as focuses and as directrices, the N_p points and the N_s straight lines on which the N_s segments lie, respectively. Finally, let T be the union of T_1, T_2, and T_3. It can be demonstrated that the medial axis of the set S is a subset of the set T and is therefore made up of linear elements and tracts of parabolas (Figure A1a).

[67] From a geometrical point of view we propose the following technique to build the skeleton. Let us consider the internal sides ℓ_k of the triangles constituting the flat region (k = 1, $N_{\ell t}$; $N_{\ell t}$ = number of triangle sides not belonging to boundary B). Since the skeleton Sk of the region S consists of tracts of bisectors, axes, and parabolas, we compute the intersections of the axes, bisectors, and parabolas of the set T with all the internal triangle sides ℓ_k. For each side ℓ_k of a triangle of S, there is therefore a set I_k that consists of these intersection points. However, for each set I_k, one and only one of these points belongs to the skeleton of S. This point can be easily identified since it is at maximum distance from all the boundary segments of region S (Figure A1b). Sk$_k$ indicates the set of these points (one for each triangle side ℓ_k) belonging to the skeleton of

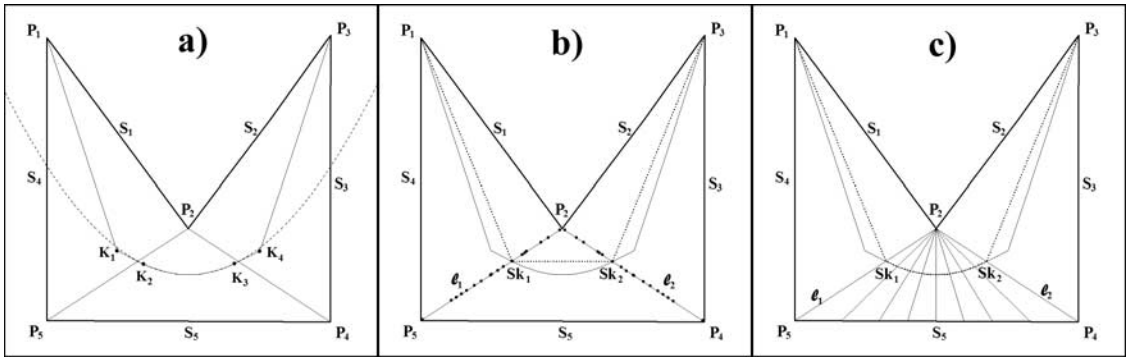

Figure A1. (a) Points P_1, P_2, P_3, P_4, P_5 are the nodes of a digitized contour line (segments S_1, S_2, S_3, S_4, S_5). The Delaunay triangles are $P_1P_2P_5$, $P_2P_4P_5$, and $P_2P_3P_4$. The skeleton of the region is the polyline $P_1K_1K_2K_3K_4P_3$, where P_1K_1 is the bisector of the angle with sides S_1 and S_4, K_1K_2 is the bisector of the angle with sides S_1 and S_5, K_2K_3 is the arc of parabola with focus in P_2 and directrix S_5, and so on. (b) The intersections (set I_1) of the segment P_2P_5 (ℓ_1) with the set T are shown as bold dots. In the set I_1, one and only one point belongs to the skeleton (point Sk_1). This point can be easy identified since it has a maximum distance from all the boundary segments of the region. The digital approximation (dotted line in Figure A1b) of the real skeleton (continuous line) is obtained by connecting all the points Sk_k (in the Figure A1b, points Sk_1 and Sk_2). (c) To improve the digitized approximation of the skeleton, new internal triangle sides ℓ_k can be added so that, for example, the segment Sk_1Sk_2 is improved to a polyline.

Sk. By joining the points Sk_k of contiguous triangles, we can reconstruct a digital approximation of the skeleton of the region S (Figure A1b). This approximation has been referred to in this paper as the inferred breakline (IB) (Figure A1b). To obtain a better approximation of the digitalized skeleton to the real one, the number of Sk_k points can be arbitrarily increased, adding additional internal triangles and sides ℓ_k (Figure A1c).

[68] Calculation of the medial axis is subject to problems of noise when using digital contour lines since the shape and length of the skeleton strictly depends on the approximation with which the original line is digitized. Furthermore, the greater the accuracy of the digitization (high number of contour points, i.e., shorter segments), the greater the "noise." For example, the skeleton of an ellipse-shaped contour line joins the two points of maximum curvature (Figure A2a). As shown in Figure A2b, the digital approximation of the contour increases the number of segments of the skeleton, and this number further increases with an improvement in the digital approximation of the ellipse (Figure A2c). In order to obtain the significant tract of the medial axis only, we have to identify the extreme points of the principal IB (departure-arrival point (DAP) of the IB). These coincide with points of local maximum curvature of the contour line and can be easily identified, as shown in Figures A3a and A3b. The DAP is the triangle vertex with sides belonging to the same contour line (in this case, all the triangle vertices are consecutive points on the same contour line: dark gray triangles in Figures A3a and A3b). In order to select the original skeleton only and ignore the noise introduced by digitization, we need to consider only the branches of the medial axes coming from triangles with consecutive vertices on the same contour line (DAP). The main skeleton selected in this way is known as the "principal skeleton" (PS). PS is a subset of the digital skeleton and approximates the skeleton of the original continuous contour line.

Appendix B: Principal Skeleton by DEST

[69] The computation of the principal skeleton starts from the DAP of the DGTs. To reduce computational time, a left branch (LB) and right branch (RB) are identified, starting from DAP, along the contour, until (1) the vertices of a LGT (the set of boundary segments QAE and QBF, respectively, in Figure 5) or (2) a not horizontal triangle is encountered (i.e., the green triangle FEQ_3 of Figure 6, where points E and F belong to a contour line, while point Q_3 belongs to another one). The IB connects a set of points Sk_I on the internal sides of the flat triangles of region R. As shown in Figure 5, it is simple to verify that for each internal side AB,

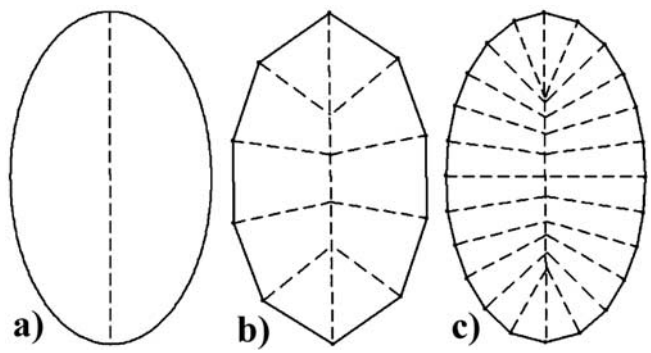

Figure A2. (a) Skeleton of an ellipse is the dashed segment joining the points of maximum curvature. (b–c) If the ellipse is approximated by a set of segments (digitalized contour), new branches add to the medial axis (dashed segments). Their number increases as the number of segments approximating the contour increases.

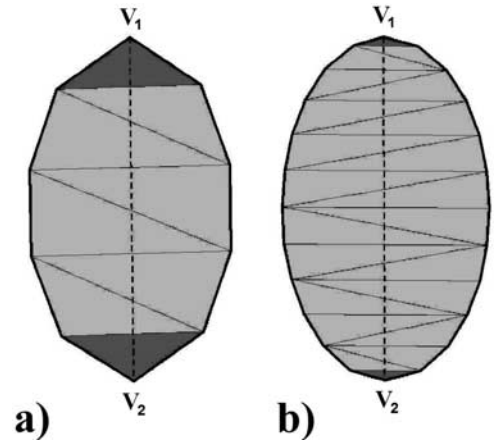

Figure A3. In order to obtain the medial axis, the extreme points of the principal IB have to be identified (departure-arrival points (DAP) of the IB: points V_1 and V_2). They coincide with points of local maximum curvature of the contour line and can be easily identified since they are the vertices of those triangles with two sides belonging to the same contour line (dark gray triangles).

the point Sk_{AB} of the skeleton belongs to the set I_{AB} of all the intersections of the segment AB with a subset T_{SD} of T. While T takes account of all the possible unions, T_{SD} is made up of elements belonging to opposite branches (for example, bisectors of angles with sides lying on two boundary segments of LB and RB, respectively). From a computational point of view the skeletal point Sk_{AB} of the segment AB is simply evaluated as the point of the set I_{AB} at equal distance from the two branches LB and RB.

Notation

AB internal side of a triangle of R (the side does not belong to the contour line B).
B boundary of R (also track of a contour line bordering a flat region).
CDT constrained Delaunay triangulation (some segments are forced to be sides of triangles).
DAP points of maximum curvature of B; these are also the end points on B of the IB.
DGT triangle with two sides on the contour line B; the common vertex of the two sides is a DAP.
DT Delaunay triangulation.
IB inferred breakline (the PS of B).
I_k set of intersection points of T with segment ℓ_k.
I_{AB} set of intersection points of T_{DS} with segment AB.
$\ell_k (k = 1, N_{\ell t})$ internal sides of the triangles of R.
LB boundary segments of B, clockwise following a DAP.
LGT triangle containing the intersection of three branches of the PS; no side of the triangle belongs to the contour line B.
M nearest point of B to P.
N natural numbers 0, 1, 2, 3....
$N_{\ell t}$ number of internal sides of the triangles of R.
N_s number of boundary segments of R.
N_p number of end points of boundary segments of R.
P point of R.
PM distance of point P from point M.
PS principal skeleton.
$Q_a, Q_b, Q_c...$ points of B with a maximum local curvature, and also the vertex of two contiguous sides of triangles along the contour line.
r straight line.
R flat region made up of triangles with vertices on the same contour line.
RB boundary segments of B, counterclockwise following a DAP.
S union of the N_s segments and N_p points.
Sk skeleton of S.
Sk_k point of the set I_k belonging to the skeleton of S (it is the point of maximum distance from all the N_s segments of B).
Sk_{AB} point of the segment AB belonging to the skeleton of S.
T_1 union of all the bisectors of all the pairs of straight lines on which the N_s segments lie.
T_2 union of all the axes of all the N_s segments.
T_3 union of all the parabolas with foci in the N_p points and directrices on the N_s segments.
T $T_1 \cup T_2 \cup T_3$.
T_{SD} subset of T obtained by considering only elements belonging to the LB and RB respectively (for example, the bisector of the angle formed by two straight lines one lying on a boundary segment of the LB, and another on a segment of the RB).
T triangle of R with vertices at the same quote.
x_p, y_p, z_p coordinates of point P.
V region of the plane.
WHT triangle simply crossed by the IB; one side of the triangle lies on the contour line B.

[70] **Acknowledgments.** This work was partially supported by GNV-INGV and by the Italian Ministry of the Environment. We greatly thank the two reviewers, George Hilley and George Wadge, for better motivating our work. As a result of these very useful suggestions, the actual version of the paper has been tied more closely to the needs of the practitioner geomorphologist. We thank Ilaria Isola for providing us with contour lines of old Vesuvius and for reconstructing the TIN of the volcano by DEST. We also thank Mary Helen Dickson for improving our English.

References

Achilli, V., P. Baldi, L. Baratin, C. Bovini, E. Ercolani, S. Gandolfi, M. Anzidei, and F. Riguzzi (1998), Digital photogrammetric survey on the island of Vulcano, *Acta Vulcanol.*, *10*, 1–5.

Albani, M., and B. Klinkenberg (2003), A spatial filter for the removal of striping artefacts in digital elevation models, *Photogramm. Eng. Remote Sens.*, *69*, 755–765.

Almansa, A., F. Cao, Y. Gousseau, and B. Rougè (2002), Interpolation of digital elevation models using AMLE and related methods, *IEEE Trans. Geosci. Remote Sens.*, *40*, 314–325.

Armienti, P., and M. T. Pareschi (1987), Automatic reconstruction of surge deposit thicknesses: Applications to some Italian volcanoes, *J. Volcanol. Geotherm. Res.*, *31*, 313–320.

Arrighi, S., C. Principe, and M. Rosi (2001), Violent strombolian and subplinian eruptions at Vesuvius during post-1631 activity, *Bull. Volcanol.*, *43*, 126–150.

Bamber, J. L., S. Ekholm, and W. B. Krabill (2001), A new, high-resolution digital elevation model of Greenland fully validated with airborne laser altimeter data, *J. Geophys. Res.*, *106*, 6733–6745.

Barberi, F., M. Ghigliotti, G. Macedonio, H. Orellana, M. T. Pareschi, and M. Rosi (1992), Volcanic hazard assessment of Guagua Pichincha (Ecuador) based on past behaviour and numerical models, *J. Volcanol. Geotherm. Res.*, *49*, 53–68.

Bisson, M., M. Favalli, A. Mori, F. Mazzarini, M. T. Pareschi, and L. Sinapi (2003), A morphometric model of the Aeolian Islands (Italy), *Nuovo Cimento*, *26*, 417–435.

Blum, H. (1967), A transformation for extracting new descriptors of shape, in *Proceedings of the Symposium on Models for Perception of Speech and Visual Form*, edited by W. Whaten-Dunn, pp. 362–380, MIT Press, Cambridge, Mass.

Carrara, A., G. Bitelli, and R. Carla (1997), Comparison of techniques for generating digital terrain models from contour lines, *Int. J. Geogr. Inf. Syst.*, *11*, 451–473.

Cioni, R., R. Santacroce, and A. Sbrana (1999), Pyroclastic deposists as a guide for reconstructing the multi-stage evolution of the Somma-Vesuvius caldera, *Bull. Volcanol.*, *60*, 207–222.

Costa-Cabral, M. C., and S. J. Burges (1994), Digital elevation model networks (DEMON): A model of flow over hillslopes for computation of contributing and dispersal areas, *Water Resour. Res.*, *30*, 1681–1692.

Davis, C. H., H. Jiang, and X. Y. Wang (2001), Modeling and estimation of the spatial variation of elevation error in high resolution DEMs from stereo-image processing, *IEEE Trans. Geosci. Remote Sens.*, *39*, 2483–2489.

Eastman, J. R. (1995), Idrisi for Windows: User's guide, report, Clark Univ., Worcester, Mass.

Eastman, J. R., P. A. K. Kyem, J. Toledano, and W. Jin (1993), GIS and decision making, in *Explorations in Geographic Information Systems Technology*, vol. 4, U.N. Inst. for Training and Res., Geneva, Switzerland.

Fairfield, J., and P. Leymarie (1991), Drainage networks from grid digital elevation models, *Water Resour. Res.*, *27*, 709–717.

Favalli, M., F. Innocenti, M. T. Pareschi, G. Pascquaré, F. Mazzarini, S. Branca, L. Cavarra, and A. Tibaldi (1999), The DEM of Mt. Etna: Geomorphological and structural implications, *Geodin. Acta*, *12*, 279–290.

Florinsky, I. (1998), Accuracy of local topographic variables derived from digital elevation models, *Int. J. Geogr. Inf. Sci.*, *12*, 47–61.

Freeman, T. G. (1991), Calculating catchment area with divergent flow based on a regular grid, *Comput. Geosci.*, *17*, 413–422.

Golias, N. A., and R. W. Dutton (1997), Delaunay triangulation and 3D adaptive mesh generation, *Finite Elem. Anal. Design*, *25*, 331–341.

Gorte, B. G. H., and W. Koolhoven (1990), Interpolation between isolines based on the Borgefors distance transform, *ITC J.*, *1*, 245–247.

Guzzetti, F., and P. Reichenbach (1994), Towards a definition of topographic division of Italy, *Geomorphology*, *11*, 57–74.

Hutchinson, M. F. (1989), A new procedure for griddding elevation and stream line data with automatic removal of spurious pits, *J. Hydrol.*, *106*, 211–232.

Kirby, E., K. X. Whipple, W. Tang, and Z. Chen (2003), Distribution of active rock uplift along the eastern margin of the Tibetan Plateau: Inferences from bedrock channel longitudinal profiles, *J. Geophys. Res.*, *108*(B4), 2217, doi:10.1029/2001JB000861.

Kuhni, A., and O. A. Pfiffner (2001), The relief of the Swiss Alps and adjacent areas and its relation to lithology and structure: Topographic analysis from a 250-m DEM, *Geomorphology*, *41*, 285–307.

Lee, J. (1991), Comparison of existing methods for building triangular irregular network models of terrain from grid digital elevation models, *Int. J. Methods Eng.*, *5*, 267–285.

Li, X. Y. (2003), Generating well-shaped d-dimensional Delaunay Meshes, *Theor. Comput. Sci.*, *296*, 145–165.

Li, Z. (1994), A comparative study of the accuracy of digital terrain models (DTMs) based on various data models, *J. Photogramm. Remote Sens.*, *49*, 2–11.

Liu, H., and K. C. Jezek (1999), Investigating DEM error patterns by directional variograms and Fourier analysis, *Geophys. Anal.*, *31*, 249–266.

Liu, H., K. C. Jezek, and B. Li (1999), Development of an Antarctic digital elevation model by integrating cartographic and remotely sensed data: A geographic information system based approach, *J. Geophys. Res.*, *104*, 23,199–23,213.

Macedonio, G., and M. T. Pareschi (1991), An algorithm for the triangulation of arbitrarily distributed points: Applications to volume estimate and terrain fitting, *Comput. Geosci.*, *17*, 859–874.

Martz, L. W., and J. Garbrecht (1995), Automated reconstruction of valley lines and drainage networks from grid digital elevation models: A review and a new method: Comments, *J. Hydrol.*, *167*, 393–396.

Mavriplis, D. J. (1995), An advancing front Delaunay Triangulation algorithm designed for robustness, *J. Comput. Phys.*, *117*, 90–101.

McCullagh, M. J. (1988), Terrain and surface modelling systems: Theory and practice, *Photogramm. Record*, *12*, 747–779.

Meyer, T. H. (2000), *Terrain Analysis: Principles and Applications*, edited by J. P. Wilson and J. C. Gallant, John Wiley, Hoboken, N. J.

Mitas, L., and H. Mitasova (1999), Spatial interpolation, in *Geographical Information Systems: Principles, Techniques, Management and Applications*, edited by P. Longley et al., pp. 418–492, John Wiley, Hoboken, N. J.

Mitasova, H., J. Hofierka, M. Zlocha, and L. Iverson (1996), Modelling topographic potential for erosion and deposition using GIS, *Int. J. GIS*, *10*, 629–641.

Nazzaro, A. (1997), *Il Vesuvio: Storia Eruttiva e Teorie Vulcanologiche*, Liguori Editore, Naples, Italy.

O'Callaghan, J. F., and D. M. Mark (1984), The extraction of drainage networks from digital elevation data, *Comput. Vision Graphics Image Process.*, *28*, 59–79.

Pareschi, M. T., M. Favalli, F. Giannini, R. Sulpizio, G. Zanchetta, and R. Santacroce (2000a), May 5, 1998, debris flows in circumvesuvian areas (southern Italy): Insights for hazard assessment, *Geology*, *28*, 639–642.

Pareschi, M. T., R. Santacroce, M. Favalli, F. Giannini, M. Bisson, L. Cavarra, and A. Meriggi (2000b), *Un Gis per il Vesuvio*, Litografia Felici, Pisa, Italy.

Pareschi, M. T., R. Santacroce, R. Sulpizio, and G. Zanchetta (2002), Volcanoclastic debris flows in the Clanio Valley (Campania, Italy): Insight for the assessment of hazard potential, *Geomorphology*, *43*, 219–231.

Pavlidis, T. (1982), *Algorithms for Graphics and Image Processing*, Comput. Sci. Press, Rockville, Md.

Preparata, F. P., and M. I. Shamos (1985), *Computational Geometry*, Springer-Verlag, New York.

Quinn, P., K. J. Beven, P. Chevallier, and O. Planchon (1991), The prediction of hillslope flow paths for distributed hydrological modeling using digital terrain models, *Hydrol. Processes*, *5*, 59–80.

Rebay, S. (1993), Efficient unstructured mesh generation by means of Delaunay Triangulation and Bower-Watson algorithm, *J. Comput. Phys.*, *106*, 125–138.

Reichenbach, P., R. J. Pike, W. Acevedo, and R. K. Mark (1993), A new landform map of Italy in computer-shaded relief, *Boll. Geod. Sci. Affini, IGMI*, *LII*, 21–44.

Rosi, M., R. Santacroce, and A. Sbrana (1987), Geological map of Somma Vesuvius volcanic complex, map, scale 1:25,000, CNR PF Geodin. L. Salomone, Rome.

Shearer, J. W. (1990), The accuracy of digital terrain models, in *Terrain Modelling in Surveying and Civil Engineering*, edited by G. Petrie and T. J. M. Kennie, pp. 315–336, WPS, London.

Stevens, N. F., G. Wadge, and J. B. Murray (1999), Lava flow volume and morphology from digitized contour maps: A case study at Mount Etna, Sicily, *Geomorphology*, *28*, 251–261.

Stevens, N. F., V. Manville, and D. W. Heron (2003), The sensitivity of a volcanic flow model to digital elevation model accuracy: Experiments with digitised map contours and interferometric SAR at Ruapehu and Taranaki volcanoes, New Zealand, *J. Volcanol. Geotherm. Res.*, *119*, 89–105.

Taud, H., J. F. Parrot, and R. Alvarez (1999), DEM generation by contour line dilatation, *Comput. Geosci.*, *25*, 775–783.

Watson, D. F. (1981), Computing the N-dimensional Delaunay Tessellation with application to Voronoi polytopes, *Comput. J.*, *24*, 167–172.

Watson, D. F. (1992), *Contouring: A Guide to the Analysis and Display of Spatial Data*, Pergamon, New York.

Wolock, D. M., and C. V. Price (1994), Effects of digital elevation model map scale and data resolution on a topography-based watershed model, *Water Resour. Res.*, *30*, 3041–3052.

Wood, J. D., and P. F. Fisher (1993), Assessing interpolation accuracy in elevation models, *IEEE Comput. Graphics Appl.*, *13*, 48–56.

Zhang, W., and D. R. Montgomery (1994), Digital elevation model grid size, landscape representation, and hydrologic simulations, *Water Resour. Res.*, *30*, 1019–1028.

M. Favalli and M. T. Pareschi, Instituto Nazionale di Geofisica e Vulcanologia, Via della Faggiola 32, I-56100 Pisa, Italy. (favalli@pi.ingv.it; pareschi@pi.ingv.it)